Editors' Suggestion

Avalanches and Extreme Value Statistics of a Mesoscale Moving Contact Line

Caishan Yan,[1] Dongshi Guan,[2,3] Yin Wang,[1] Pik-Yin Lai,[4,5,*] Hsuan-Yi Chen,[4,5,†] and Penger Tong[1,‡]
[1]Department of Physics, Hong Kong University of Science and Technology, Clear Water Bay, Kowloon, Hong Kong
[2]State Key Laboratory of Nonlinear Mechanics, Institute of Mechanics, Chinese Academy of Sciences, Beijing 100190, China
[3]School of Engineering Science, University of Chinese Academy of Sciences, Beijing 100049, China
[4]Department of Physics and Center for Complex Systems, National Central University, Taoyuan City 320, Taiwan
[5]Physics Division, National Center for Theoretical Sciences, Taipei 10617, Taiwan

(Received 21 June 2023; revised 13 November 2023; accepted 16 January 2024; published 23 February 2024)

We report direct atomic force microscopy measurements of pinning-depinning dynamics of a circular moving contact line (CL) over the rough surface of a micron-sized vertical hanging glass fiber, which intersects a liquid-air interface. The measured capillary force acting on the CL exhibits sawtoothlike fluctuations, with a linear accumulation of force of slope k (stick) followed by a sharp release of force δf, which is proportional to the CL slip length. From a thorough analysis of a large volume of the stick-slip events, we find that the local maximal force F_c needed for CL depinning follows the extreme value statistics and the measured δf follows the avalanche dynamics with a power law distribution in good agreement with the Alessandro-Beatrice-Bertotti-Montorsi (ABBM) model. The experiment provides an accurate statistical description of the CL dynamics at mesoscale, which has important implications to a common class of problems involving stick-slip motion in a random defect or roughness landscape.

DOI: 10.1103/PhysRevLett.132.084003

Contact angle hysteresis (CAH), where the contact line (CL) between a liquid-air interface and a solid substrate is pinned by the physical roughness and/or chemical heterogeneities on the solid surface, is a long-standing problem in interfacial dynamics [1–4]. The CL pinning causes the contact angle θ between the liquid and solid surfaces to exhibit hysteresis, with the advancing contact angle θ_a being larger than the receding contact angle θ_r [1–3,5]. Although considerable progress has recently been made in controlling the wettability of various textured solid surfaces [6,7], the CAH that occurs on many ambient solid surfaces of interest remains poorly understood. For example, there is not yet a theoretical or experimental explanation for how CAH is determined by the basic features of the underlying pinning force field [3–5].

When a CL is pulled under a constant speed, the CL motion is accomplished by a continuous series of local pinning-depinning events, with each individual event involving a varying number of defect sites (or different slip sizes) on the solid surface. It is commonly believed that the dynamics of CL depinning involves avalanches of slip size, which give rise to a power-law distribution of the slip length [8–12]. Experimental studies of the CL dynamics are often conducted in two spatial regimes. One is at the macroscopic level, in which a CL of macroscopic length interacts with many surface defects simultaneously and thus fluctuations resulting from individual slip events are averaged out. These studies focused mainly on the mean value of the advancing and receding capillary forces (or contact angels θ_a and θ_r) [13–22]. The other is at the nanoscopic level, in which a nanoscale tip is in contact with a liquid interface [23–25]. In this case, only single-defect dynamics is at play without involving any collective effect of multiple defects, which is a key factor in avalanche dynamics [8–12]. What is lacking in the study of CL dynamics is an experimental framework at the mesoscale that is small enough to resolve the slip events at the single slip resolution but is also large enough to allow the individual slips to have a broad range of slip sizes in a well-characterized defect landscape.

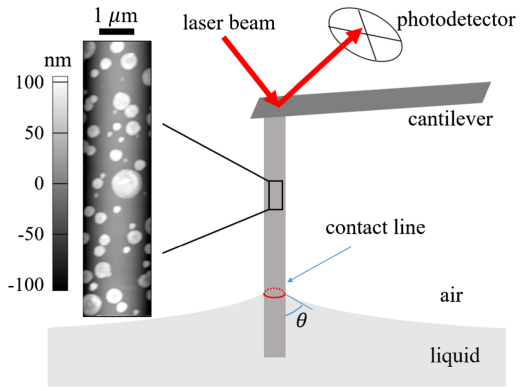

FIG. 1. Schematic of the long-needle AFM probe made of a vertical glass fiber of diameter $d \simeq 3$ μm and length ~600 μm. The glass fiber penetrates a liquid-air interface and a circular contact line is formed on the fiber surface. The inset shows a magnified AFM topographic image of a portion of the fiber covered by a variety of PTS clusters.

In this Letter, we demonstrate that the micron-sized long-needle AFM, as illustrated in Fig. 1, provides such a mesoscale experimental framework for the study of the collective depinning of a moving CL at the single-slip resolution. With this framework, we are able to provide a statistical description of the pinning-depinning dynamics at a critical state [9,12,21], which bridges the gap between the microscopic behavior of individual slips and the macroscopic laws of CAH.

Figure 1 shows the working principle of the long-needle AFM. The vertical glass fiber is glued onto the front end of a rectangular AFM cantilever and a circular CL of length πd is formed on the fiber surface when the lower fiber tip touches a liquid-air interface. The glass fiber is coated with a thin layer of propyltrichlorosilane (PTS), so that its surface becomes both physically and chemically rough with many randomly distributed PTS aggregates having a broad range of sizes, as shown in the inset of Fig. 1 (see Supplemental Material, Secs. I.A and II.A for more details [26]). In the experiment, we use the long-needle AFM to accurately measure the capillary force F acting on the circular CL [13,47–49],

$$F(z) = -\pi d\gamma \cos\theta(z), \tag{1}$$

as a function of fiber traveling distance z in the advancing (fiber moves downward) and receding (fiber moves upward) directions. Here, γ is the liquid-air interfacial tension, and the sign of F is defined as $F \leq 0$ for $\theta \leq 90°$ and $F > 0$ for $\theta > 90°$. With the fiber speed $u = 0.62$ μm/s, we find the capillary number $C_a \leq 10^{-7}$ for the fluids used and hence the viscous drag is negligibly small compared to the capillary force. Our AFM measurements are, therefore, conducted at the low speed (or static) limit (see Supplemental Material, Secs. I and III.A for more experimental details [26]).

Figure 2(a) shows two typical hysteresis loops of $F(z)$ when the fiber is first pushed downward (advancing) and then pulled upward (receding) for two liquid interfaces. At the beginning, the fiber was partially immersed in the liquid and the CL was pinned on the fiber surface. As the fiber starts to advance (or recede), the pinned liquid-air interface is stretched, causing a linear increase (or decrease) in $F(z)$, as shown by the left (or right) side of the hysteresis loop. The slope k_0, which is proportional to γ, defines the static spring constant of the liquid interface [5]. When the elastic restoring force exceeds the maximal pinning force, the CL depins and begins to move, giving rise to steady-state fluctuations of $F(z)$. Figure 2(b) shows a magnified view of the steady-state zigzag curve of $F(z)$, which has a sawtoothlike shape with a slow accumulation of force (pinning or stick) followed by a sharp force release (depinning or slip). The local stick-slip events are characterized by three quantities, k, F_c, and δf, as marked in Fig. 2(b). The slope k of the linear force accumulation

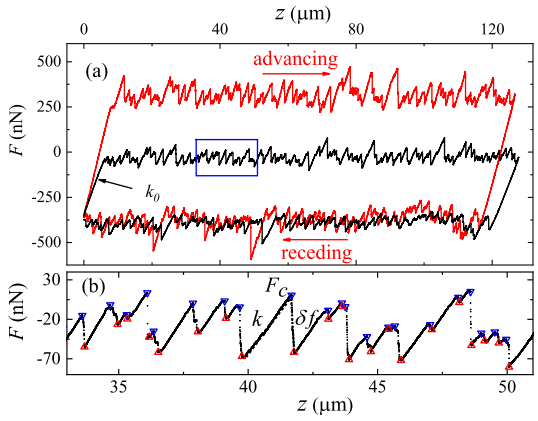

FIG. 2. (a) Measured capillary force $F(z)$ as a function of vertical displacement z of the fiber, when it is pushed downward (advancing) and is pulled upward (receding) through a liquid interface. The red curve is obtained for a water-air interface and the black curve is obtained with the same fiber segment in contact with an ethylene-glycol-air interface. All the measurements are made when the fiber moves at a constant speed $u = 0.62$ μm/s. (b) A magnified view of the black curve marked in the blue box in (a). The blue downward and red upward triangles mark, respectively, the beginning and end of each slip event of the CL.

defines the dynamic spring constant of the moving CL. The local maximal force F_c is the critical depinning force needed for the onset of slip, at which a segment of the CL slips off from the pinning sites with a sudden release of force δf. As the CL sweeps over the PTS-coated fiber surface, the stick and slip cycles repeat with k, F_c, and δf all showing significant fluctuations (see Supplemental Material, Sec. II.B for more details [26]).

Figure 3 shows the measured probability density function (PDF) $P(f_c)$ of the normalized maximal force $f_c = (F_c - \langle F_c\rangle)/\sigma_{F_c}$, where $\langle F_c\rangle$ and σ_{F_c} are, respectively, the mean and root-mean-squared values of F_c. The measured PDFs $P(f_c)$ for a given fiber but with different liquids overlap with each other, suggesting that the measured $P(f_c)$ is an intrinsic property of the fiber surface and is insensitive to the liquids used. All the measured PDFs $P(f_c)$ can be well described by the generalized extreme value (GEV) distribution [50],

$$P(f_c) = \frac{1}{\beta}(1+\xi y)^{-(1+1/\xi)} e^{-(1+\xi y)^{-1/\xi}}, \tag{2}$$

where $y = (f_c - \mu)/\beta$ with $\mu = \beta[1-\Gamma(1-\xi)]/\xi$, $\beta = |\xi|/\sqrt{\Gamma(1-2\xi) - \Gamma^2(1-\xi)}$, and $\Gamma(\ldots)$ being the gamma function. Equation (2) is used to model the distribution of extreme values in a sequence of independent and identically distributed random variables with zero mean and unity variance. The solid lines in Fig. 3 show the fits of Eq. (2) to the data with only one fitting parameter ξ. For the two fibers used, we find $\xi = -0.17$ (black line) and $\xi = -0.06$ (red line).

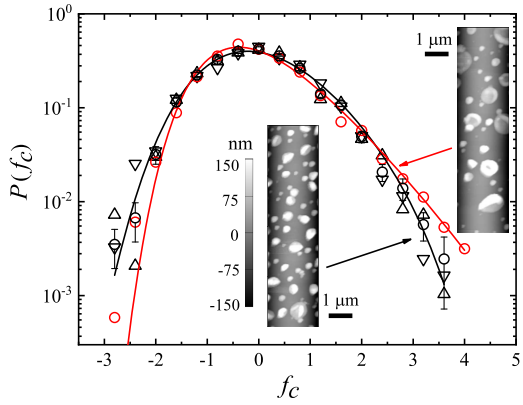

FIG. 3. Measured PDFs $P(f_c)$ of the normalized maximal force f_c. The black symbols are obtained using the same PTS-coated fiber with three different liquids: water (upward triangles), 66 wt.% glycerol aqueous solution (downward triangles) and ethylene glycol (circles). The red circles are obtained using a different PTS-coated fiber with ethylene glycol. The four sets of data are all obtained in the advancing direction at $u = 0.62$ μm/s. For each set of data, the measured $F(z)$ recorded approximately 2500 slip events over a traveling distance $z \simeq 500$ μm. The black and red solid lines show the fits of Eq. (2) to the black and red circles, respectively, with $\xi = -0.17 \pm 0.04$ (black line) and $\xi = -0.06 \pm 0.04$ (red line). Insets show the AFM topographic images of the two PTS-coated fiber surfaces used and the vertical gray-scale bar applies to both AFM images.

For $\xi < 0$, Eq. (2) is reduced to the reversed Weibull distribution that has an upper bound $(f_c)_M = \mu - \beta/\xi$ beyond which $P(f_c) = 0$. This means the local maximal force has an upper bound, $(F_c)_M = [(f_c)_M]\sigma_{F_c} + \langle F_c \rangle$. Note that the measured F_c [and hence $(F_c)_M$] by AFM contains an equilibrium contribution, $F_{\rm eq} = -\pi d\gamma \cos\theta_0$, when the fiber surface has no defect [see Eq. (1) and Supplemental Material Sec. III.A for details [26])]. For the two sets of data obtained with different fibers but with the same liquid, we find their net roughness-induced maximal force, $(F_c)'_M = (F_c)_M - F_{\rm eq}$, differs considerably with $(F_c)'_M \simeq 402$ nN for the black circles and $(F_c)'_M \simeq 750$ nN for the red circles. This difference in $(F_c)'_M$ is correlated with the actual morphology of the fiber surface. As shown in the insets of Fig. 3, the fiber surface with a larger variation of defect sizes (right image) yields a wider distribution in $P(f_c)$ (red circles) and a larger upper bound $(F_c)'_M$. This is because large defects tend to pin the CL more firmly compared with small ones, and they are responsible for producing larger values of f_c and thus dominate the tail part of $P(f_c)$. For $\xi = 0$, Eq. (2) is reduced to the Gumbel distribution, which has an exponential tail with an infinite upper bound $[(f_c)_M \to \infty]$. Evidently, the red circles shown in Fig. 3 are not far from this limit. The extreme value statistics for F_c has been predicted in a previous theoretical calculation [10].

When the CL sweeps over the fiber surface, a sudden slip of the CL takes place only locally over a CL segment where the defect-induced pinning force can no longer balance the continuously increasing elastic restoring force from the stretched liquid interface. The force release δf for a local slip can be written as

$$\delta f = \int_0^{\pi d} dx\{h[x; z_i(x)] - h[x; z_f(x)]\} = -\langle \partial_z h \rangle_A \pi d \Delta z_{\rm slip} \simeq k_0 \Delta z_{\rm slip}, \quad (3)$$

where $h(x; z)$ is the defect-induced heterogeneous interfacial tension difference between the solid-air and solid-liquid interfaces (with x being in the direction along the CL), $z_i(x)$ and $z_f(x)$ are, respectively, the CL positions before and after the slip. In the above, $\Delta z_{\rm slip} = (1/\pi d)\iint_A dxdz$ is the center-of-mass displacement of the CL during the slip, and $\langle \ldots \rangle_A$ denotes an averaged over the area A enclosed by $z_i(x)$ and $z_f(x)$ (see inset of Fig. 4). The third equality of Eq. (3) results from the onset condition for a local slip to occur, when the slope k_0 of the external pulling force becomes equal to the local (downward) slope $|\langle \partial_z h \rangle_A| \pi d$ of the defect-induced pinning force field [51–53]. Indeed, we find that this onset condition is satisfied during the CL slip (see Supplemental Material, Sec. III.B for more details [26]).

Using Eq. (3), we obtain the slip length $\Delta z_{\rm slip} = \delta f / k_0$ for each slip event and its PDF $P(\Delta z_{\rm slip})$ is shown in Fig. 4. It is found that the measured PDFs for fibers with different surface roughnesses and in contact with different liquids overlap with each other and can be described by a common power law,

$$P(\Delta z_{\rm slip}) \sim (\Delta z_{\rm slip})^{-\epsilon}, \quad (4)$$

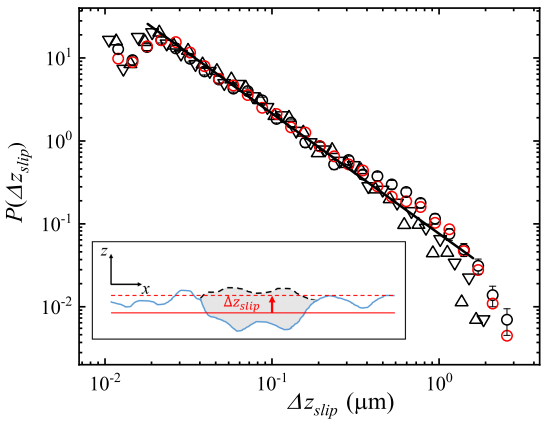

FIG. 4. Log-log plot of the measured PDFs $P(\Delta z_{\rm slip})$ of the slip length $\Delta z_{\rm slip}$. The four sets of data are obtained using the same force trajectories and with the same symbols as those used in Fig. 3. The solid line shows a fit of Eq. (4) to the data points with the power-law exponent $\epsilon = 1.45 \pm 0.10$. The inset shows a sketch of a local slip of the CL, with the blue solid line and black dashed line indicating, respectively, the CL positions before and after the slip. The red solid and dashed lines show the corresponding center-of-mass positions of the CL.

with the power-law exponent $\epsilon = 1.45 \pm 0.10$. This result demonstrates that CL stick-slip indeed involves avalanche dynamics, which gives rise to a broad range of slip lengths without a characteristic value [8,10–12]. The power-law exponent ϵ quantifies the relative incidence between the large-sized and small-sized slips, i.e., more large-sized slips are detected for a smaller value of ϵ, and vice versa. Figure 4 reveals that the value of ϵ remains unchanged for fibers with different roughnesses and in contact with different liquids studied.

When a mesoscale CL moves over the fiber surface, it interacts with a finite number of defects (roughly 10–100) and its stick-slip involves multiple defects. For example, when a strong defect slips, it releases a large stress, which is partially transferred to its neighboring defects and triggers their slips. This avalanche process is described by the ABBM model [8,10–12], which predicts $\epsilon = 3/2$ at the low speed limit. Figure 4 thus provides a direct verification of the ABBM model at the single slip resolution (see Supplemental Material, Sec. III.C for more details [26]).

We now discuss the statistics of the dynamic spring constant k. The inset of Fig. 5 shows the measured PDF $P(k)$ of the normalized variable k/k_0. Here k_0 is the static spring constant when the CL is completely pinned, as shown in Fig. 2(a). It is seen that the four sets of data have a similar shape, once k is normalized by k_0. The measured k varies in the range $0.3 \lesssim k/k_0 \lesssim 1.1$ and is peaked around $k/k_0 \simeq 0.94$, which indicates that k_0 sets a cutoff value for k. This result suggests that the CL is often partially pinned and its local (microscopic) movement allows the CL to feel a local (upward) force gradient (or spring constant) k' resulting from the defect landscape $h(x;z)$.

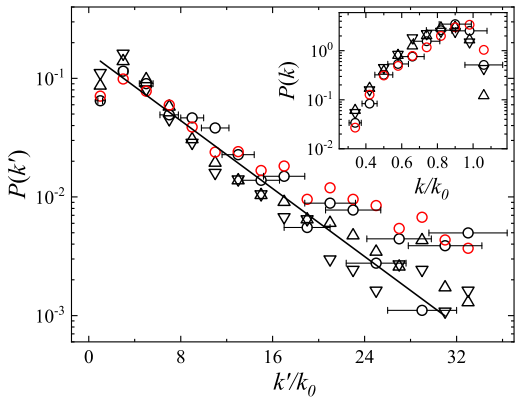

FIG. 5. Measured PDF $P(k')$ of the local gradient k' of the pinning force field. In the plot, the value of k' is normalized by k_0. The solid line shows a fit of Eq. (6) to the black symbols with $b = 0.165 \pm 0.015$. Inset shows the measured PDF $P(k)$ of the dynamic spring constant k normalized by k_0. The four sets of data in the main figure and inset are all obtained from the same force trajectories and with the same symbols as those used in Fig. 3. The error bars show the experimental uncertainties of the measurements.

With a local balance between the pinning force $F_{\rm pin} = \int_0^{\pi d} h[x; z_{cl}(x)]dx$ and the elastic restoring force of the liquid interface, we find

$$\frac{1}{k} = \frac{1}{k'} + \frac{1}{k_0}, \tag{5}$$

where $k' = dF_{\rm pin}/d\bar{z}_{cl} > 0$ ($\bar{z}_{cl} = (1/\pi d)\int_0^{\pi d} z_{cl}(x)dx$ is the mean position of the CL (see Supplemental Material Sec. III.B for details [26]). Equation (5) states that the dynamic spring constant k comes from two springs connected in series; one is from the pinning force field $F_{\rm pin}(z)$ with the spring constant k' and the other is from the liquid-air interface with the static spring constant k_0. As the CL sweeps over the PTS-coated fiber surface, it feels different values of k'. Equation (5) indicates that k has an upper bound k_0 when the CL is completely pinned ($k' \to \infty$), which explains the variation range of the measured k.

With Eq. (5), one can extract the local force gradient k' from the measured k and its PDF $P(k')$ is shown in Fig. 5. It is found that the measured PDFs $P(k')$ for fibers with different surface roughnesses can all be well described by an exponential distribution,

$$P(k') = be^{-b(k'/k_0)}, \tag{6}$$

where b is the only fitting parameter. The value of b is a measure of the width of the distribution and also determines the mean value of k', i.e., $\langle k' \rangle/k_0 = 1/b$. From the fitting result (solid line), we find $\langle k' \rangle/k_0 = 1/b \simeq 6.1$ for black symbols. For another fiber with a larger surface roughness (red circles), its mean force gradient $\langle k' \rangle/k_0$ has a slightly larger value, as expected.

Joanny and de Gennes [53] proposed that the pinning-depinning transition (or the onset of hysteresis) of a CL takes place when $\langle k' \rangle/k_0 > (2\pi/e)^{1/2} \simeq 1.52$. The fitting result shown in Fig. 5 thus reveals that this onset condition is satisfied for the moving CLs. Our result that the measured $\langle k' \rangle/k_0$ is approximately four times larger than the onset requirement indicates that the CLs studied here are in the strong pinning regime for stick-slip. Exponential-like PDFs, which fall off much slower than a Gaussian, were also observed in various dynamically heterogenous or spatially disordered systems [54,55]. From the measured PDFs $P(h)$ of the surface roughness height $h(z)$ and its power spectrum density functions $S(q)$ (see Supplemental Material, Fig. S3), we find that the PTS clusters (defects) on the fiber surface have a wide range of heights and lateral sizes, which gives rise to a broad distribution of the local force gradient k'. Figures 5 and S3, therefore, reveal a statistical connection between the surface roughness landscape and the underlying pinning force field (see Supplemental Material Sec. II.A for details [26]).

Equations (2)–(6) thus provide a statistical description of the stick-slip dynamics of a moving CL at the critical state. In particular, we find that the measured PDFs of the slip

length Δz_{slip}, the maximal force F_c needed to trigger local slips, and the local force gradient k' of the pinning force field are statistically interconnected. The broad distribution of k' indicates that the avalanche dynamics of the CL is caused primarily by fluctuations in the pinning force field. Slips with a larger slip length are lower-probability events, which require a larger value of k' (or larger defects) to hold the local CL segments and a larger value of F_c to depin them, both have a lower probability in their distributions. Our experiment verifies the prediction of the ABBM model, which used a Brownian-correlated pinning force field to describe the stick-slip motion of the CL.

The authors wish to thank Dr. P. Le Doussal for useful discussions. This work was supported in part by RGC of Hong Kong under Grants No. 16300920 (P. T.) and No. 16300421 (P. T.), by the NSFC of China under the Grant No. 11972351 (D. G.), and by MoST of Taiwan under the Grants No. 110-2112-M-008-026-MY3 (P. Y. L.) and No. 110-2112-M-008-030- (H. Y. C.).

*Corresponding author: hschen@phy.ncu.edu.tw
†Corresponding author: pylai@phy.ncu.edu.tw
‡Corresponding author: penger@ust.hk

[1] P.-G. de Gennes, Wetting: Statics and dynamics, Rev. Mod. Phys. **57**, 827 (1985).
[2] L. Leger and J.-F. Joanny, Liquid spreading, Rep. Prog. Phys. **55**, 431 (1992).
[3] D. Bonn, J. Eggers, J. Indekeu, J. Meunier, and E. Rolley, Wetting and spreading, Rev. Mod. Phys. **81**, 739 (2009).
[4] J. Snoeijer and B. Andreotti, Moving contact lines: Scales, regimes, and dynamical transitions, Annu. Rev. Fluid Mech. **45**, 269 (2013).
[5] Y. J. Wang, S. Guo, H.-Y. Chen, and P. Tong, Understanding contact angle hysteresis on an ambient solid surface, Phys. Rev. E **93**, 052802 (2016).
[6] D. Quéré, Wetting and roughness, Annu. Rev. Mater. Res. **38**, 71 (2008).
[7] T.-L. Sun, L. Feng, X.-F. Gao, and L. Jiang, Bioinspired surfaces with special wettability, Acc. Chem. Res. **38**, 644 (2005).
[8] F. Colaiori, Exactly solvable model of avalanches dynamics for Barkhausen crackling noise, Adv. Phys. **57**, 287 (2008).
[9] L.-H. Tang, *Collective Transport and Depinning in Encyclopedia of Complexity and Systems Science*, edited by R. A. Meyers (Springer, New York, 2009).
[10] P. Le Doussal and K. J. Wiese, Driven particle in a random landscape: Disorder correlator, avalanche distribution, and extreme value statistics of records, Phys. Rev. E **79**, 051105 (2009).
[11] M. LeBlanc, L. Angheluta, K. Dahmen, and N. Goldenfeld, Distribution of maximum velocities in avalanches near the depinning transition, Phys. Rev. Lett. **109**, 105702 (2012).
[12] M. LeBlanc, L. Angheluta, K. Dahmen, and N. Goldenfeld, Universal fluctuations and extreme statistics of avalanches near the depinning transition, Phys. Rev. E **87**, 022126 (2013).
[13] J.-M. Di Meglio and D. Quéré, Contact angle hysteresis: A first analysis of the noise of the creeping motion of the contact line, Europhys. Lett. **11**, 163 (1990).
[14] J.-M. Di Meglio, Contact angle hysteresis and interacting surface defects, Europhys. Lett. **17**, 607 (1992).
[15] G. D. Nadkarni and S. Garoff, An investigation of microscopic aspects of contact angle hysteresis: Pinning of the contact line on a single defect, Europhys. Lett. **20**, 523 (1992).
[16] A. Paterson, M. Fermigier, P. Jenffer, and L. Limat, Wetting on heterogeneous surfaces: Experiments in an imperfect Hele-Shaw cell, Phys. Rev. E **51**, 1291 (1995).
[17] S. Moulinet, A. Rosso, W. Krauth, and E. Rolley, Width distribution of contact lines on a disordered substrate, Phys. Rev. E **69**, 035103(R) (2004).
[18] C. Priest, R. Sedev, and J. Ralston, Asymmetric wetting hysteresis on chemical defects, Phys. Rev. Lett. **99**, 026103 (2007).
[19] M. Reyssat and D. Quéré, Contact angle hysteresis generated by strong dilute defects, J. Phys. Chem. B **113**, 3906 (2009).
[20] P. Le Doussal, K. J. Wiese, S. Moulinet, and E. Rolley, Height fluctuations of a contact line, Europhys. Lett. **87**, 56001 (2009).
[21] S. Varagnolo, D. Ferraro, P. Fantinel, M. Pierno, G. Mistura, G. Amati, L. Biferale, and M. Sbragaglia, Stick-slip sliding of water drops on chemically heterogeneous surfaces, Phys. Rev. Lett. **111**, 066101 (2013).
[22] H. Perrin, R. Lhermerout, K. Davitt, E. Rolley, and B. Andreotti, Defects at the nanoscale impact contact line motion at all scales, Phys. Rev. Lett. **116**, 184502 (2016).
[23] S. M. M. Ramos, E. Charlaix, A. Benyagoub, and M. Toulemonde, Wetting on nanorough surfaces, Phys. Rev. E **67**, 031604 (2003).
[24] S. Ramos and A. Tanguy, Pinning-depinning of the contact line on nanorough surfaces, Eur. Phys. J. E **19**, 433 (2006).
[25] M. Delmas, M. Monthioux, and T. Ondarcuhu, Contact angle hysteresis at the nanometer scale, Phys. Rev. Lett. **106**, 136102 (2011).
[26] See Supplemental Material at http://link.aps.org/supplemental/10.1103/PhysRevLett.132.084003 for more details, which includes Refs. [27–46].
[27] M. E. Mcgovern, K. M. R. Kallury, and M. Tomposon, Role of solvent on the silanization of glass with octadecyltrichlorosilane, Langmuir **10**, 3607 (1994).
[28] A. Y. Fadeev and T. J. McCarthy, Self-assembly is not the only reaction possible between alkyltrichlorosilanes and surfaces: Monomolecular and oligomeric covalently attached layers of dichloro- and trichloroalkylsilanes on silicon, Langmuir **16**, 7268 (2000).
[29] D. S. Guan, Y. J. Wang, E. Charlaix, and P. Tong, Asymmetric and speed-dependent capillary force hysteresis and relaxation of a suddenly stopped moving contact line, Phys. Rev. Lett. **116**, 066102 (2016).
[30] Physical constants of organic compounds, in *CRC Handbook of Chemistry and Physics, Internet Version 2005*, edited by D. R. Lide (CRC Press, Boca Raton, 2005).

[31] K. Takamura, H. Fischer, and N. R. Morrow, Physical properties of aqueous glycerol solutions, J. Pet. Sci. Eng. **98**, 50 (2012).
[32] M. L. Sheely, Glycerol viscosity tables, Ind. Eng. Chem. **24**, 1060 (1932).
[33] J. L. Hutter and J. Bechhoefer, Calibration of atomic-force microscope tips, Rev. Sci. Instrum. **64**, 1868 (1993).
[34] B. N. J. Persson, O. Albohr, U. Tartaglino, A. I. Volokitin, and E. Tosatti, On the nature of surface roughness with application to contact mechanics, sealing, rubber friction and adhesion, J. Phys. Condens. Matter **17**, R1 (2005).
[35] A. Gujrati, S. R. Khanal, L. Pastewka, and T. D. B. Jacobs, Combining TEM, AFM, and profilometry for quantitative topography characterization across all scales, ACS Appl. Mater. Interfaces **10**, 29169 (2018).
[36] T. D. B. Jacobs, T. Junge, and L. Pastewka, Quantitative characterization of surface topography using spectral analysis, Surf. Topogr. **5**, 013001 (2017).
[37] A. Gujrati, A. Sanner, S. R. Khanal, N. Moldovan, H. Zeng, L. Pastewka, and T. D. B. Jacobs, Comprehensive topography characterization of polycrystalline diamond coatings, Surf. Topogr. **9**, 014003 (2021).
[38] B. Alessandro, C. Beatrice, G. Bertotti, and A. Montorsi, Domain-wall dynamics and Barkhausen effect in metallic ferromagnetic materials. II. Experiments, J. Appl. Phys. **68**, 2901 (1990).
[39] S. Guo, M. Gao, X. Xiong, Y. J. Wang, X.-P. Wang, P. Sheng, and P. Tong, Direct measurement of friction of a fluctuating contact line, Phys. Rev. Lett. **111**, 026101 (2013).
[40] S. Guo, C.-H. Lee, P. Sheng, and P. Tong, Measurement of contact-line dissipation in a nanometer-thin soap film, Phys. Rev. E **91**, 012404 (2015).
[41] A. Carlson, G. Bellani, and G. Amberg, Contact line dissipation in short-time dynamic wetting, Europhys. Lett. **97**, 44004 (2012).
[42] Q. Vo and T. Tran, Contact line friction of electrowetting actuated viscous droplets, Phys. Rev. E **97**, 063101 (2018).
[43] X. Li, F. Bodziony, M. Yin, H. Marschall, R. Berger, and H. J. Butt, Kinetic drop friction, Nat. Commun. **14**, 4571 (2023).
[44] A. Prevost, E. Rolley, and C. Guthmann, Dynamics of a helium-4 meniscus on a strongly disordered cesium substrate, Phys. Rev. B **65**, 064517 (2002).
[45] S. Guo, Y.-J. Wang, H.-Y. Chen, and P. Tong, Wetting dynamics of a lipid monolayer, Langmuir **37**, 4879 (2021).
[46] P.-G. de Gennes, F. Brochard-Wyart, and D. Quéré, in *Capillarity and Wetting Phenomena* (Springer, New York, USA, 2004), p. 89.
[47] X.-M. Xiong, S. Guo, Z.-L. Xu, P. Sheng, and P. Tong, Development of an atomic-force-microscope-based hanging-fiber rheometer for interfacial microrheology, Phys. Rev. E **80**, 061604 (2009).
[48] D. Guan, Y. J. Wang, E. Charlaix, and P. Tong, Simultaneous observation of asymmetric speed-dependent capillary force hysteresis and slow relaxation of a suddenly stopped moving contact line, Phys. Rev. E **94**, 042802 (2016).
[49] D. Guan, E. Charlaix, and P. Tong, State and rate dependent contact line dynamics over an aging soft surface, Phys. Rev. Lett. **124**, 188003 (2020).
[50] M. R. Leadbetter, G. Lindgren, and H. Rootzén, *Extremes and Related Properties of Random Sequences and Processes* (Springer, New York, USA, 2004), p. 267.
[51] L. Prandtl and Z. Angew, A thought model for the kinetic theory of solids, J. Appl. Math. Mech. **8**, 85 (1928).
[52] G. A. Tomlinson, A molecular theory of friction, Philos. Mag. Ser. 5 **7**, 905 (1929).
[53] J.-F. Joanny and P.-G. de Gennes, A model for contact angle hysteresis, J. Chem. Phys. **81**, 552 (1984).
[54] W. He, H. Song, Y. Su, L. Geng, B. J. Ackerson, H. B. Peng, and P. Tong, Dynamic heterogeneity and non-Gaussian statistics for acetylcholine receptors on live cell membrane, Nat. Commun. **7**, 11701 (2016).
[55] X.-Z. He, Y. Wang, and P. Tong, Dynamic heterogeneity and conditional statistics of non-Gaussian temperature fluctuations in turbulent thermal convection, Phys. Rev. Fluids **3**, 052401(R) (2018).